Electronic Supplementary Information

Temperature-Programmed Desorption of Large Molecules: Influence of Thin Film Structure and Origin of Intermolecular Repulsion

Pierre-Martin Dombrowski [a,†], Stefan R. Kachel [b,†], Leonard Neuhaus [b], J. Michael Gottfried [b], Gregor Witte [a,]*

a Fachbereich Physik, Philipps-Universität Marburg, Renthof 7, 35032 Marburg, Germany

b Fachbereich Chemie, Philipps-Universität Marburg, Hans-Meerwein-Straße 4, 35032 Marburg, Germany

*E-Mail: gregor.witte@physik.uni-marburg.de

†P.-M.D. and S.R.K. contributed equally to this work.

Contents

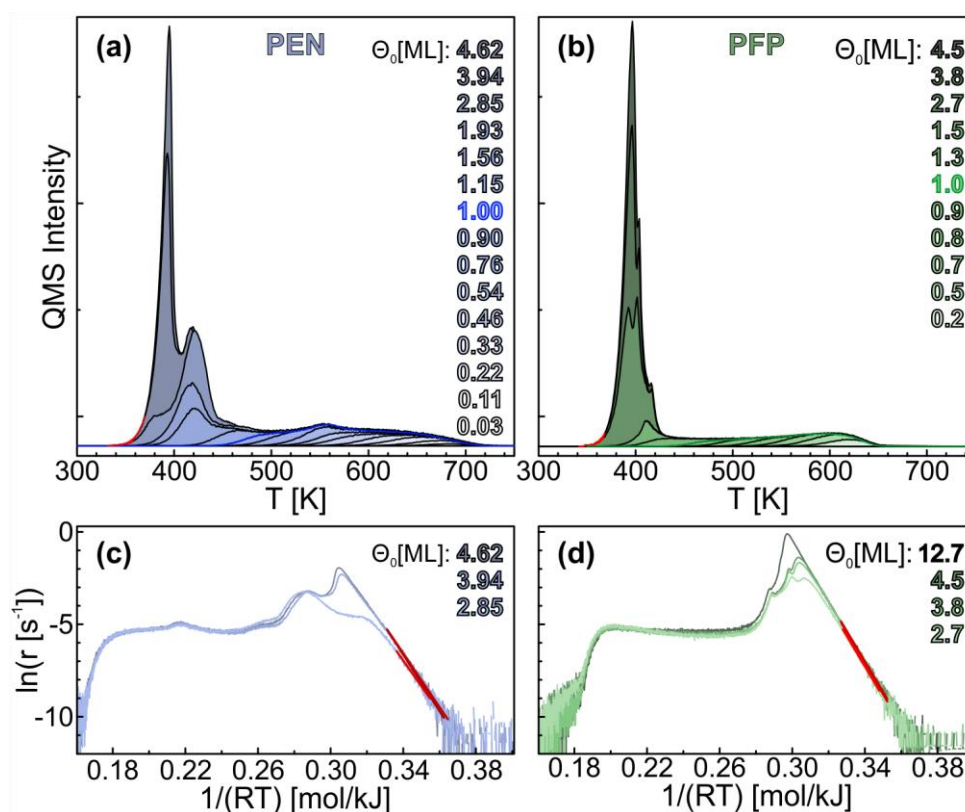## 1. Analysis of multilayer TPD traces of PEN/Au(111) and PFP/Au(111)

Fig. S1: LEA results for PEN/Au(111) (left) and PFP/Au(111) (right). (a) and (b) TPD traces (PEN: *m/z* = 278 amu, PFP: *m/z*= 530 amu, β = 1 K/s) of films with varying initial coverages Θ$_0$ ranging from 0.03 ML to 4.6 ML. The data used for the LEA (only multilayer films) is highlighted in red. (c) and (d) Corresponding Arrhenius plots with linear fits in red. Note that the given initial coverages correspond to the calibration for the flat-lying monolayers. In the multilayers, molecules adopt a herringbone packing, so the given coverages are not perfectly accurate.

Figs. S1 (a) and (b) show TPD traces of PEN/Au(111) and PFP/Au(111), respectively, for initial coverages up to 4.6 ML. In both cases, we observe two distinct multilayer peaks: one at higher temperatures that saturates at initial coverages in the bilayer-regime, and one at lower temperatures that shows the typical multilayer characteristics. The saturation of the high-temperature multilayer peak at coverages < 2.9 ML in the case of PEN strongly suggests that it corresponds to a stabilized second molecular layer. Such distinct signals attributed to desorption from the second molecular layer have already been reported for other molecules adsorbed on Au(111),[S1,S2] which indicates that molecules in the second layer experience some additional interaction with the substrate. Note that, while the first layers of PEN/Au(111) and PFP/Au(111) adopt a perfectly lying orientation, subsequent layers grow in a herringbone structure. [S3,S4] Our coverage-normalization therefore only holds for the first layer, and can be expected to overestimate the coverage for multilayers due to their increased lateral packing density. This explains the saturation of the bilayer peak at a supposed coverages of more than 2 ML.

To quantitatively analyze the multilayer TPD traces, we have performed a leading edge analysis (LEA) according to:

$$\ln(r) = \ln(\nu) - \frac{E_{\text{des}}}{RT} . \qquad (S1)$$

Using eqn S1, the kinetic parameters can be determined from a linear regression around the leading edge in Arrhenius plots of $\ln(r)$ vs. $(RT)^{-1}$. This assumes desorption kinetics of zeroth order (cf. eqn 1, n = 0). The Arrhenius plots in Figs. S1 (c) and (d) show clear linear behaviour of our data in the range of the leading edge, which validates this assumption. The leading edge (fit results highlighted in red in Figs. 1 (c) and (d)) are summarized in Tab. S1.

Coverage [ML]	E_{des} [kJ/mol]	ν [s^{-1}]
PEN/Au(111)		
2.9	142.0 ± 4.7	$10^{17.9 \pm 0.7}$
3.9	145.7 ± 2.2	$10^{18.7 \pm 0.3}$
4.6	146.4 ± 4.1	$10^{18.1 \pm 0.6}$
PFP/Au(111)		
3.4	166.0 ± 2.3	$10^{21.3 \pm 0.3}$
4.8	168.2 ± 2.1	$10^{21.8 \pm 0.3}$
5.7	162.3 ± 2.0	$10^{20.9 \pm 0.3}$
12.7	164.8 ± 1.9	$10^{21.2 \pm 0.3}$

Tab. S1: Kinetic parameters for multilayers of PEN/Au(111) and PFP/Au(111) according to Fig. S1. Note that, as explained above, multilayer coverages are not calibrated accurately and over-estimated.

In the bilayer regime, desorption kinetics are more complex than in subsequent multilayers. Not only does the leading edge of the bilayer desorption signal shift to lower temperatures with increasing coverage, in contrast to the common leading edge for all multilayer desorption traces due to zeroth-order desorption kinetics, but the bilayer desorption peak also has a shoulder (feature β in the main paper). These more complex desorption kinetics are likely to be caused by a coverage-dependent change of the adsorption geometry in the second layer. In contrast to the first layer which absorbs in a coplanar on the Au(111) surface, all subsequent layers grow in a herringbone packing motif.[S3] However, at low coverages in the second layer, molecules might still adopt a coplanar orientation with respect to the first molecular layer, so that a transition to the herringbone packing motif must occur during bilayer growth. Because of this structural reconfiguration, we refrain from a quantitative analysis of the bilayer desorption signal.

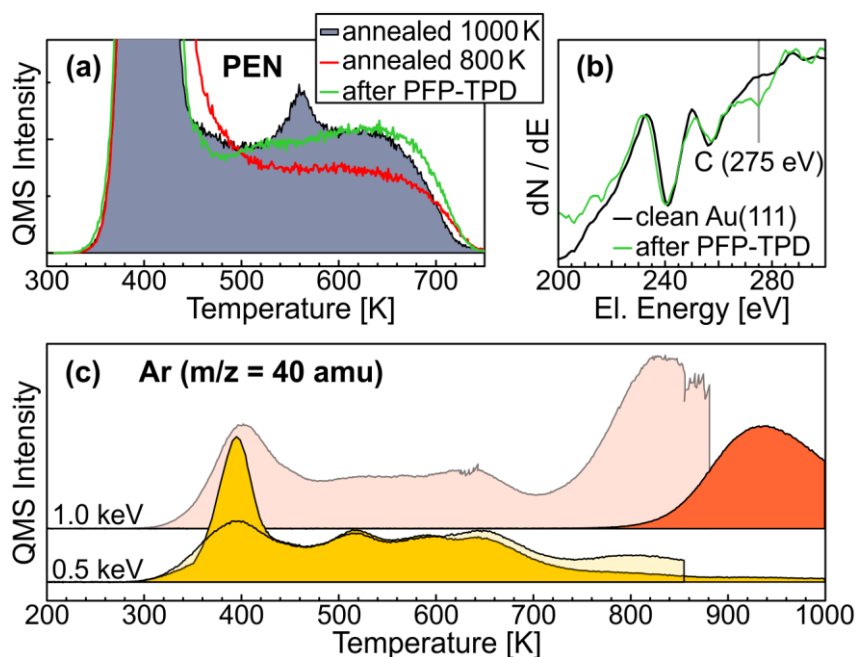## 2. Preparation of the Substrate and Decomposition of PFP

Fig. S2: (a) Multilayer TPD traces of PEN/Au(111) (m/z = 278 amu, β = 1 K/s) of differently prepared Au(111) substrates: sputtered (room temperature, 0.5 keV) and subsequently annealed at 800 K (red line), sputtered and subsequently annealed at 1000 K (filled blue trace) and after a TPD experiment with PFP/Au(111) without sputtering prior to the deposition of PEN (green line). (b) AES data (electron energy 2 keV) of a clean Au(111) surface and of a contaminated surface after a TPD experiment with PFP/Au(111). (c) TPD traces of Ar (m/z= 40 amu, β = 1 K/s) for Au(111) substrates sputtered at 300 K with an ion energy of 1.0 keV (orange traces) or 0.5 keV (yellow traces). The transparent traces were recorded prior to the non-transparent ones, but heating was stopped at approximately 850 K. Afterwards, the non-transparent traces were recorded from the same sample.

Fig. S2 (a) shows TPD traces of multilayers of PEN/Au(111) that were recorded for differently prepared Au(111) substrates. If the substrate is sputtered (at room temperature with an ion energy of 0.5 keV) and subsequently annealed at 1000 K, we observe the shape of the TPD traces that is discussed in the main paper. In particular, the distinct maximum of the (sub-) monolayer TPD traces around 560 K, caused by the activation of the degree of freedom of molecular rotation, is present. However, we find that said maximum does not appear if TPD experiments with PFP have been conducted on the same substrate earlier and the substrate was not sputter-cleaned prior to the deposition of PEN, i.e., the substrate was only annealed (green line in Fig. S2 (a)). This stands in contrast to subsequent TPD experiments with PEN/Au(111), where the maximum at 560 K occurs even without sputtering of the substrate between the experiments (provided the crystal was well-prepared earlier) as long as no PFP is deposited onto the Au(111) crystal. Note that for all TPD experiments shown in the main paper and this ESI, the Au(111) substrate was nonetheless sputtered and annealed after every TPD experiment so that the substrate surface is always well-defined.

As discussed in the main paper, PFP decomposes partially during TPD experiments. The finding that prior TPD experiments with PFP alter the desorption kinetics of PEN suggests that, upon decomposition of PFP, carbon residues remain on the surface even after annealing up to more than 800 K. This is corroborated by AES measurements (cf. Fig. S2 (b)) that show a carbon signal after TPD experiments with PFP. It appears that these carbon residues can only be removed from the substrate surface by sputter-cleaning. Thus, we can conclude that the characteristic maximum of the (sub-) monolayer TPD traces of PEN/Au(111) occurs only if the substrate is well-prepared and clean.

Interestingly, we find that the maximum at 560 K of the PEN/Au(111) TPD traces also disappears if the substrate is only annealed at 800 K after sputtering with a kinetic energy of 0.5 keV (red trace in Fig. S2 (a)). To investigate on the influence of the annealing temperature of the substrate prior to the deposition of PEN on the PEN/Au(111) TPD traces, we recorded the Argon desorption signal (m/z=40 amu) from a supposedly pristine Au(111) substrate (cf. Fig. S2 (c)). For Au(111) crystals sputtered with Ar at room temperature with a kinetic energy of 1.0 keV, we find a significant Ar desorption signal even at temperatures larger than 750 K at which PEN would not be found on the crystal in a PEN/Au(111) TPD experiment (orange traces). If the Au(111) crystal is annealed up to almost 900 K (transparent orange trace), we still find desorption of Ar from the crystal in subsequent TPD experiments (non-transparent orange trace). This indicates that, during sputtering, some Ar intercalates into the Au(111) crystal, as reported for various noble gas and metal combinations in previous studies.[S5–S7] Ar located below the Au(111) surface might create defects that lead to altered desorption kinetics of PEN/Au(111), similar to the influence of carbon residues caused by decomposed PFP.

If we reduce the kinetic energy of the ions to 0.5 keV (yellow traces), we find a reduced Ar signal, indicating that less Ar intercalates into the Au(111) crystal. However, annealing of the Au(111) crystal after sputtering to 850 K is not sufficient to remove Ar completely from the crystal. Only at approximately 900 K, Ar desorption becomes negligible and Ar can be considered mostly removed from the Au(111) crystal. With this preparation protocol, we obtain the characteristic maximum of the PEN/Au(111) TPD traces. If we compare the two yellow TPD traces in Fig. S2 (c), we also find that the intensity of the first Ar desorption peak increases upon annealing to 850 K. Since phases with a smaller desorption energy and therefore lower desorption temperature are likely to be located closer to the crystal surface,[S5] this indicates that insufficient annealing leads to an accumulation of Ar near the Au(111) surface, as more deeply intercalated Ar diffuses towards the crystal surface, which increases the number of potential surface defects.

3. Description of the modified leading edge analysis

As discussed in the main paper, thermally activated desorption can be described by the Polanyi-Wigner equation (cf. eqn 1). For first order desorption kinetics (n=1) that describe (sub-) monolayer desorption of PEN/Au(111) and PFP/Au(111) accurately (cf. Fig. S3), eqn 1 can be rewritten as

$$\ln\left(\frac{r}{\Theta}\right) = \ln(\nu) - \frac{E_{\mathrm{des}}}{RT} \qquad \text{(S2)}$$

where r is the measured rate of desorption, Θ is the current surface coverage, R is the molar gas constant and T is the surface temperature. To simplify the following discussion, we define new variables $y = \ln(r/\Theta)$ and $x = (RT)^{-1}$. Assuming that the kinetic parameters are constant, i.e. independent of the surface coverage Θ, one can determine the kinetic parameters from a linear fit $y(x) = mx + n$. Then, the slope of the fitted function is $m = -E_{\mathrm{des}}$ and the intercept is $n = \ln(\nu)$.

In general, the slope is given by [S8]

$$m = \frac{\partial y}{\partial x} = \frac{\partial \ln(r/\Theta)}{\partial(1/(RT))} = -E_{\mathrm{des}} + R\frac{\partial \Theta}{\partial(T^{-1})}\left[\frac{\partial \ln(\nu)}{\partial \Theta} - \frac{1}{RT}\frac{\partial E_{\mathrm{des}}}{\partial \Theta}\right]. \qquad \text{(S3)}$$

Consequently, if the kinetic parameters depend on the surface coverage, the above discussed linear relation is not fulfilled in general. The assumption of a linear relation in cases where it is not fulfilled leads to a forced compensation effect, i.e. an artificial correlation of the kinetic parameters so that the braced term in eqn S3 is zero, which is discussed in detail in other studies.[S8,S9] Only in regions of small coverage change, $\partial\Theta/\partial(T^{-1})$ is negligibly small so that a linear relation of x and y can be assumed.[S8] This is why we chose a very small coverage-range at the very onset of the TPD traces to determine the kinetic parameters for the given initial coverage from eqn S2. Although this reduces the statistical accuracy of the analysis, as only a small range of low signal-to-noise ratio of the TPD traces is used, it is of paramount importance for a reliable determination of the kinetic parameters.

To ensure reproducibility of our analysis, it was completely automated. Therefore, an algorithm was created to find an x-range / a temperature range at the low-temperature onset of each TPD trace in which eqn S2 is fulfilled:

i) **Lower x-limit:** By integration of the measured desorption rate, we can determine the temperature-dependent surface coverage that is given by

$$\Theta(T) = \Theta_0 - \frac{1}{\beta}\int_0^T r(\tilde{T})\,d\tilde{T} \qquad \text{(S4)}$$

where $\Theta_0 = \Theta(T = 0)$ is the initial surface coverage of the molecular film. We define the lower x-limit, x_1, via the temperature T_1 that fulfills $\Theta(T_1) = \Theta_0 - \Delta\Theta$. For $\Delta\Theta$, we chose $\Delta\Theta$=0.005 ML. The fact that our results for PEN/Au(111) show no evidence for a compensation effect validates our analysis, showing that $\Delta\Theta$ is sufficiently small to justify the neglect of $\partial\Theta/\partial(T^{-1})$ in eqn S3.[S8]

ii)   **Upper x-limit:** We use the first N values of a TPD trace prior to the onset of desorption to determine a background noise level $y_0 \pm \sigma_{y_0}$ as follows:

$$y_0 = \frac{1}{N} \sum_{i=1}^{N} y(x_i) \qquad \text{(S5)}$$

$$\sigma_{y_0} = \sqrt{\frac{\sum_{i=1}^{N}(y(x_i) - y_0)^2}{N(N-1)}} \qquad \text{(S6)}$$

We then chose the upper x-limit, x_0, so that

$$y(x) \geq y_0 + 3\sigma_{y_0} \quad \forall\, x \leq x_0 \; . \qquad \text{(S7)}$$

In other words, we search for the lowest temperature (largest x) at which notable desorption occurs that differs significantly from the background noise level with the additional requirement that y is at least equally large for all higher temperatures (smaller x).

We chose N = 50 to determine y_0 and σ_{y_0}, which corresponds to surface temperatures of approximately 200 K to 250 K at which desorption of PEN and PFP can be excluded.

iii)   **Linear Regression:** Lastly, we perform a linear regression of $y(x)$ in the range of $[x_0, x_1]$. As described above, the kinetic parameters can thus be determined from slope and intercept of the modelled linear function.

This algorithm was applied for the analysis of all (sub-) monolayer TPD traces with equal parameters N and $\Delta\Theta$. The results of the mLEA are shown in Fig. S3. Panels (a) and (b) show the (sub-) monolayer TPD traces of PEN/Au(111) and PFP/Au(111), respectively. The data that is used for the mLEA is highlighted by a red line for each trace. Figs. S3 (c) and (d) show the corresponding Arrhenius plots of y over x with the linear fit in red. The resulting kinetic parameters are shown in Figs. S3 (e) and (f) as well as Tab. S2.

Note that, due to the issue of molecular decomposition of PFP/Au(111) during desorption that is discussed in the main paper, the corresponding kinetic parameters are of limited accuracy. This is because the competing process of decomposition alters the measured desorption rate and thus the surface coverage that is determined from the TPD traces. Moreover, residues of decomposed PFP on the Au(111) substrate might alter the desorption kinetics of intact molecules. Nonetheless, we believe that the kinetic parameters determined for the saturated monolayer are reliable, since molecular decomposition is unlikely to occur at temperatures below 450 K as shown by a previous X-ray photoelectron spectroscopy study.[S10]
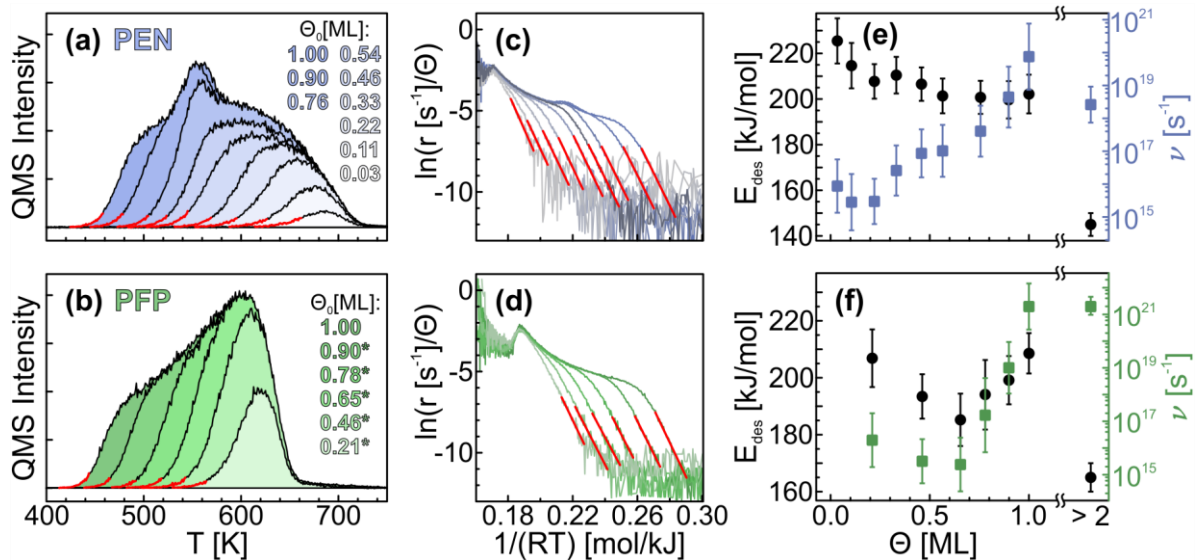
Fig. S3: mLEA fits and results for PEN/Au(111) (top row) and PFP/Au(111) (bottom row). (a) and (b) TPD traces (PEN: m/z = 278 amu, PFP: m/z = 530 amu, β = 1 K/s) with data that is used for the mLEA highlighted in red. (c) and (d) Corresponding Arrhenius plots with linear fits in red. (e) and (f) Kinetic parameters as determined from the mLEA together with those of the multilayers (Θ_0 > 2 ML). Note that in the case of PFP/Au(111), the given coverage does not take molecular decomposition into account. Submonolayer coverages for PFP/Au(111) are marked with asterisks because these values do not describe the total initial PFP coverages, but rather the fractions of the initial coverages that eventually desorb (expressed in monolayer equivalents).

Coverage [ML]	E_{des} [kJ/mol]	ν [s^{-1}]
PEN/Au(111)		
0.03	225.4 ± 9.9	$10^{15.94 \pm 0.81}$
0.11	214.6 ± 9.9	$10^{15.45 \pm 0.86}$
0.22	207.7 ± 7.6	$10^{15.47 \pm 0.69}$
0.33	210.5 ± 8.0	$10^{16.41 \pm 0.77}$
0.46	206.5 ± 7.3	$10^{16.93 \pm 0.73}$
0.54	201.4 ± 7.6	$10^{17.01 \pm 0.79}$
0.76	200.7 ± 7.3	$10^{17.61 \pm 0.78}$
0.90	199.7 ± 8.2	$10^{18.65 \pm 0.93}$
1.00	201.4 ± 8.5	$10^{19.9 \pm 1.0}$
PFP/Au(111)		
0.21*	207 ± 10	$10^{16.29 \pm 0.97}$
0.46*	193.4 ± 7.8	$10^{15.50 \pm 0.79}$
0.65*	185.2 ± 9.2	$10^{15.38 \pm 0.96}$
0.78*	194 ± 13	$10^{17.2 \pm 1.4}$
0.90*	199.1 ± 8.5	$10^{18.99 \pm 0.98}$
1.00	208.6 ± 7.1	$10^{21.30 \pm 0.87}$

Tab. S2: Kinetic parameters for (sub-) monolayers of PEN/Au(111) and PFP/Au(111). Submonolayer coverages for PFP/Au(111) are marked with an asterisk to highlight that they should not be considered accurate due to the issue of partial molecular decomposition during desorption.
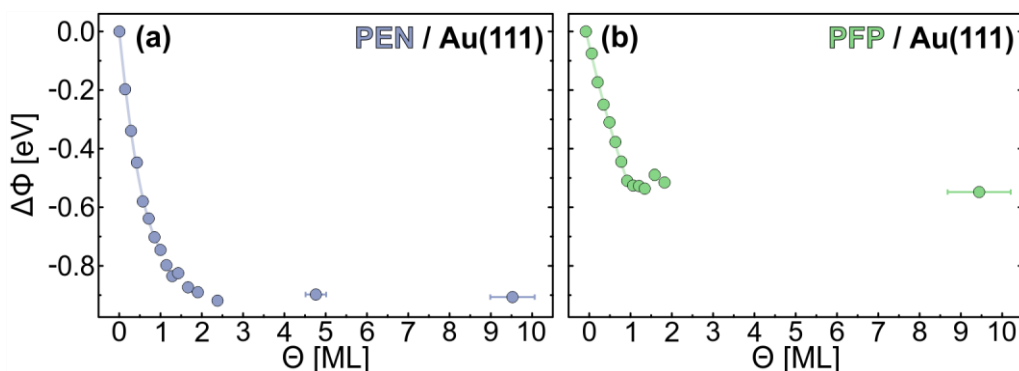
4. Complete work function data

Fig. S4: Work function change of the Au(111) surface as a function of (a) PEN and (b) PFP surface coverage.[S11] Solid lines show fits of eqn 3 in the monolayer regime.

Although the work function changes of PEN/Au(111) and PFP/Au(111) were only discussed in the monolayer regime in the main paper, we have measured the coverage-dependent work function change up to nominal coverages of several nanometres. The complete data is shown in Fig. S4.

For PEN, we find that the work function decreases with increasing coverage even after saturation of the monolayer up to a coverage of approximately 3 ML. At higher coverages, the work function remains constant. Such effects have already been observed and discussed in detail in other studies.[S12,S13] While the work function change for the saturated monolayer is only (-0.75±0.05) eV, we find a maximum work function change of (-0.92±0.05) eV for multilayers of PEN/Au(111), in agreement with previous UPS data.[S13,S14]

In contrast, the work function of PFP/Au(111) does not change further upon saturation of the molecular monolayer. It remains constant at a value of (-0.51±0.05) eV, in agreement with UPS data.[S13]

5. Calculation of lattice sum Λ and dipole-dipole interaction energy $E_{dip}(\Theta)$

As discussed in the main paper, the coverage-dependent work function change in the monolayer regime is given by

$$\Delta\Phi(\Theta) = -\frac{e}{\varepsilon_0}\frac{\mu_0 n_{\mathrm{ML}}\Theta}{1 + \alpha\Lambda\Theta^{3/2}} \qquad (S8)$$

as derived in detail by Macdonald and Barlow.[S15] The term $\Lambda\Theta^{3/2}$ describes the coverage dependence of the dipole-dipole interaction energy that scales with the third power of the inverse intermolecular distance $r_k(\Theta)$: [S15,S16]

$$\Lambda\Theta^{3/2} = \sum_k \frac{1}{r_k^3(\Theta)} \qquad (S9)$$

Here, summation is done over all neighbors of a given molecule / interface dipole. Eqns S8 and S9 assume that the adsorbates adopt a uniformly spaced adlayer structure so that $r_k(\Theta)$ increases with decreasing coverage. This holds only for adsorbates that predominantly interact repulsively and thus favor large distances to neighboring adsorbates. Then, the available surface area per molecules is proportional to Θ^{-1}. For attractive interadsorbate interactions, for instance in mixed films of PEN and PFP, island formation is likely and this model does not hold.

In the condensed monolayer, PEN/Au(111) and PFP/Au(111) adopt an oblique unit cell that, in the following, will be described by three parameters: The two axes a and b with $a \approx 2b$ and the angle γ between them. Eqn S8 was derived for quadratic or triangular unit cells for which equal scaling of the two axes of the unit cell with coverage can be assumed so that $r_i(\Theta) \propto \Theta^{-1/2}$. This yields the factor of $\Theta^{3/2}$ in eqns S8 and S9 as well as constant Λ. Since a and b are distinctly different for PEN/Au(111) as well as PFP/Au(111), it is unlikely that both axes scale equally with the surface coverage. Moreover, γ might be a function of Θ. This greatly complicates the calculation of the lattice sum in eqn S9. Since we do not how the unit cell scales exactly with Θ, we therefore assume that $a(\Theta) = a_{\mathrm{ML}}\Theta^{-1/2}$, $b(\Theta) = b_{\mathrm{ML}}\Theta^{-1/2}$ and $\gamma(\Theta) = \gamma_{\mathrm{ML}}$ where a_{ML}, b_{ML} and γ_{ML} are the unit cell parameters of the condensed monolayer. With this assumption, eqn S9 yields

$$\Lambda = \sum_k \frac{1}{r_{\mathrm{ML},k}^3} \qquad (S10)$$

where $r_{\mathrm{ML},k}$ is the distance of the k-th neighbor to a given molecule in the condensed monolayer. For an oblique unit cell, we can separate the surface into two axes and four quadrants and obtain

$$\Lambda = 2\left(\frac{1}{a_{\mathrm{ML}}^3} + \frac{1}{b_{\mathrm{ML}}^3}\right)\sum_{k=1}^{\infty}\frac{1}{k^3} + 4\sum_{l,m\geq 1}^{\infty}[(la_{\mathrm{ML}})^2 + (mb_{\mathrm{ML}})^2 + 2lma_{\mathrm{ML}}b_{\mathrm{ML}}\cos\gamma]^{-3/2}. \qquad (S11)$$

The first sum is also known as Apéry's constant $\sum_{k=1}^{\infty}k^{-3} = \zeta(3) \approx 1.2021$. The second sum has to be calculated numerically. Thus, we find $\Lambda = 7.89 \cdot 10^{-3}$ Å^{-3} for PEN and $\Lambda = 5.42 \cdot 10^{-3}$ Å^{-3} for PFP.

With this parameter, we can determine the electrostatic interaction energy of two equal and equally oriented dipoles that is given by

$$E_{\mu\mu} = \frac{1}{2\pi\varepsilon_0}\frac{\mu^2}{r_{\mu\mu}^3} \qquad (S12)$$

for a large distance $r_{\mu\mu}$.[S16] Since the minimum center-to-center distance of two molecules is 8 Å in the condensed monolayer and larger at smaller surface coverages, this assumption should hold reasonably well for our model.

From eqn S8 follows a coverage-dependent interface dipole moment of

$$\mu(\Theta) = \frac{\mu_0}{1 + \alpha\Lambda\Theta^{3/2}} \qquad (S13)$$

and thus

$$E_{\mu\mu}(\Theta) = \frac{1}{2\pi\varepsilon_0}\left(\frac{\mu_0}{1 + \alpha\Lambda\Theta^{3/2}}\right)^2\frac{1}{r_{\mu\mu}^3(\Theta)} \qquad (S14)$$

for the interaction of two interface dipoles.

To obtain the total electrostatic dipole-dipole interaction energy for a particular molecule, $E_{\mathrm{dip}}(\Theta)$, we have to calculate the lattice sum $\sum_k r_k^{-3}(\Theta)$. With eqn S9, we find

$$E_{\mathrm{dip}}(\Theta) = \frac{\Lambda\Theta^{3/2}}{2\pi\varepsilon_0}\left(\frac{\mu_0}{1 + \alpha\Lambda\Theta^{3/2}}\right)^2. \qquad (S15)$$

Thus, we can calculate the coverage-dependent interface dipole interaction energy from Λ (using the known unit cell parameters of the condensed monolayer) and μ_0 and α that can be determined from work function measurements.

6. Calculation of E_{vdW}(1 ML)

The van der Waals interaction energy E_{vdW} was calculated for the saturated monolayer as described in Ref. S17. These interactions include attractive London dispersion forces, Pauli repulsion and Coulomb interactions of the intramolecular charge distributions. The former two interactions can be described by a potential [S17]

$$E_{ij}^{\text{Pauli, London}} = a_{ij} \exp(-b_{ij}\, r_{ij}) - \frac{c_{ij}}{r_{ij}^6} \qquad (S16)$$

For the interaction of two atoms i and j. The element-specific parameters a_{ij}, b_{ij} and c_{ij} are given in Tab. S3 for C-C, H-H and C-H interactions.

Elements	a [kJ/mol]	b [Å^{-1}]	c [kJ/mol]
C-C	$3.28 \cdot 10^6$	4.59	1515
H-H	$4.17 \cdot 10^4$	4.52	189
C-H	$3.70 \cdot 10^5$	4.55	535

Tab. S3: Coefficients for Pauli and London interactions (cf. eqn S16) according to Ref. S17.

For Coulomb interactions, we have performed a Mulliken population analysis that attributes a charge to each atom of the molecule.[S18] The underlying density functional theory calculations were carried out with an aug-cc-pVTZ basis set using the B3LYP functional as implemented in the US GAMESS-code.[S19,S20] The atomic coordinates and charges according to the Mulliken population analysis are given in Tab. S4 for a PEN molecule. The atomic labels correspond to Fig. S5. For Coulomb interactions, a Coulomb potential

$$E_{ij}^{\text{Coulomb}} = \frac{1}{4\pi\varepsilon_0} \frac{q_i q_j}{r_{ij}} \qquad (S17)$$

was used.

The total van der Waals interaction energy of two atoms is then given by $E_{ij}^{\text{vdW}} = E_{ij}^{\text{Pauli, London}} + E_{ij}^{\text{Coulomb}}$. The van der Waals interaction energy acting on a single molecule can then be calculated by summation of the pair interactions of all atoms of the given molecule with all atoms of the surrounding molecules. For the saturated monolayer, we have arranged 121 molecules according to the $\left(\begin{smallmatrix} 6 & -1 \\ -2 & 3 \end{smallmatrix}\right)$ superstructure of the saturated monolayer of PEN/Au(111) and calculated the interaction energy for the centre molecule. A further increase of the number of molecules yields no notable change of the result.

Atom Nr.	Element	Coordinates		Charge [e]
		x [Å]	y [Å]	
1	C	0.000	1.407	-0.223
2	C	1.225	0.728	0.200
3	C	2.465	1.406	-0.648
4	C	3.673	0.727	0.738
5	C	4.936	1.409	-0.482
6	C	6.109	0.716	-0.399
7	H	0.000	2.493	0.129
8	H	2.465	2.492	0.047
9	H	4.936	2.494	0.220
10	H	7.055	1.245	0.371

Tab. S4: Atomic coordinates and corresponding charges determined from a Mulliken population analysis for a PEN molecule. Atomic labels correspond to Fig. S5.
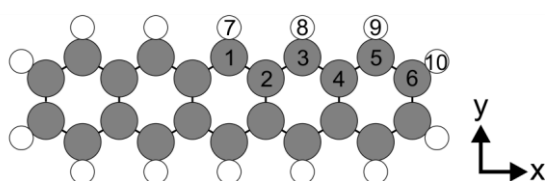

Fig. S5: PEN molecule with atomic labels for Tab. S4.

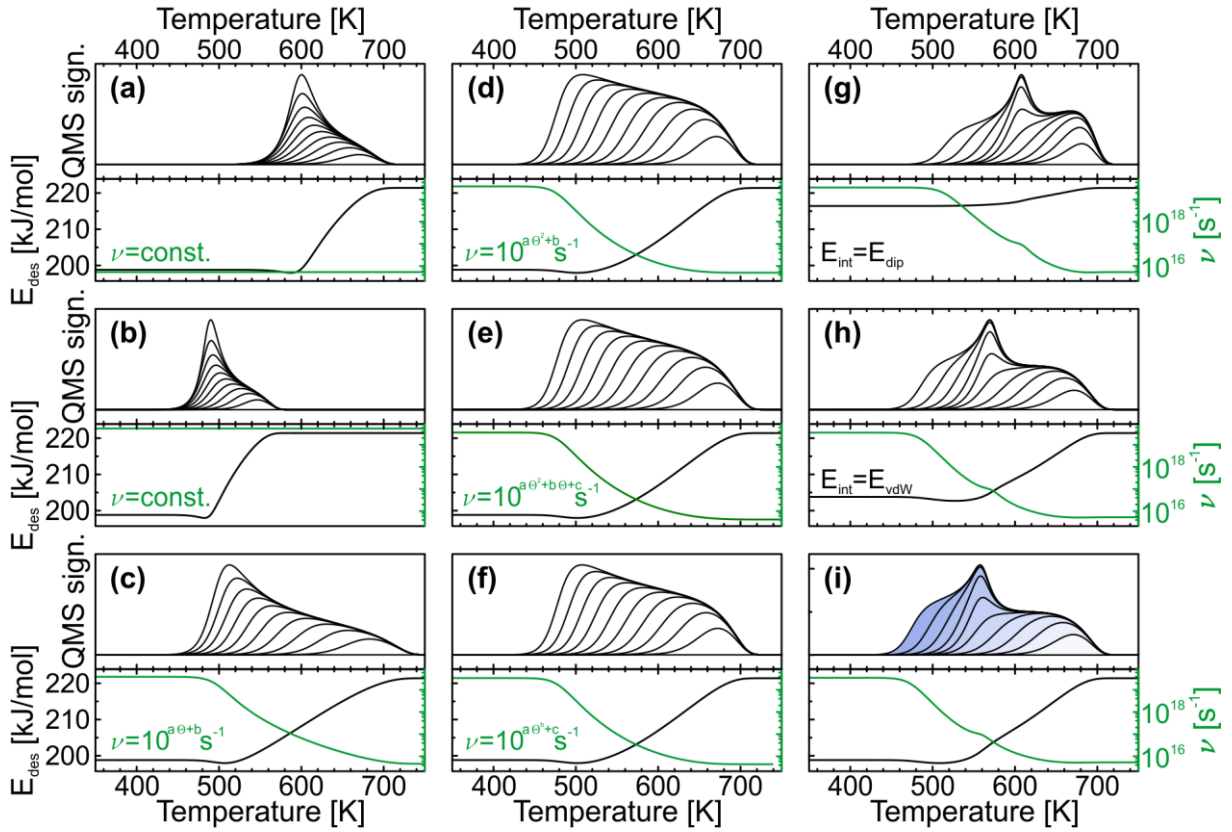# 7. Simulated TPD traces for different kinetic parameters

Fig. S6: Simulated (sub-) monolayer TPD traces of PEN/Au(111) (top) for different kinetic parameters (bottom). In the bottom panels, the temperature-dependent desorption energy is shown in black whereas the prefactor is shown in green. The text in the bottom panels indicates which of the two kinetic parameters is varied with respect to the most accurate simulation that is shown in panel (i). In the first two columns (a-f), different prefactors are chosen while the desorption energy is the same as the experimentally determined one. In the third column (g-i), the same prefactor is used as in the main paper, but the desorption energy is varied.

As discussed in the main paper, we have simulated TPD traces for different kinetic parameters to show that only a kink in the prefactor function can produce the experimentally observed shape of the TPD traces. The most accurate simulation that is also discussed in the main paper is shown in Fig. S6 (i).

For the simulated traces in Fig. S6 (a) and (b), we have assumed a constant prefactor in combination with the experimentally determined desorption energy $E_{\mathrm{des}}(\Theta) = E_0 - E_{\mathrm{int}}(\Theta)$ where $E_{\mathrm{int}}(\Theta) = E_{\mathrm{dip}}(\Theta) + E_{\mathrm{vdW}}(\Theta)$ includes interface dipole and van der Waals interactions. The corresponding TPD traces are much less broad then the experimentally observed traces and do not feature a sharp maximum at intermediate coverages. We have chosen two different constant prefactors of $\nu=10^{15.7}$ s^{-1} and $\nu=10^{19.7}$ s^{-1} for Figs. S6 (a) and (b), respectively, to illustrate the influence of the magnitude of the prefactor on the TPD traces: Clearly, a larger prefactor leads to drastically reduced desorption temperature and a reduced width of the TPD traces. This example further invalidates the arbitrary choice of prefactors for Redhead's method,[S21] as the choice of ν drastically affects results for E_{des}.

Figs. S6 (c)-(f) show simulated TPD traces with different coverage-dependent prefactors and the experimentally determined desorption energy. We have fitted a linear function (c), a quadratic function (d), a second-order polynomial (e) and an exponential function of the form $a\Theta^b + c$ (f) to the experimental results for $\log_{10}(\nu(\Theta))$ and find qualitatively very similar TPD traces. Although the temperature-range of the experimental TPD traces can be reproduced, no sharp maximum is formed at intermediate coverages.

Finally, Figs. S6 (g)-(i) show simulated TPD traces with different models for the desorption energy and a prefactor of

$$\nu(\Theta) = \frac{10^{15.7-0.5\Theta+5.8\Theta^2}}{1 + e^{-20(\Theta_c-\Theta)}} s^{-1} + \frac{10^{19.7-11.1\Theta+10.9\Theta^2}}{1 + e^{20(\Theta_c-\Theta)}} s^{-1}$$

$$\approx \begin{cases} 10^{15.7-0.5\Theta+5.8\Theta^2} s^{-1} & , \quad \Theta \leq \Theta_c \\ 10^{19.7-11.1\Theta+10.9\Theta^2} s^{-1} & , \quad \Theta > \Theta_c \end{cases}$$

with Θ_c=0.51 ML. The first expression that is used for the simulations uses logistic functions to smooth the transition between the two coverage regions. In Fig. S6 (g), only interface dipole interactions are considered, whereas in Fig. S6 (h), those interactions are ignored and only vdW interactions are modelled. In Fig. S6 (i), both interactions are considered as in the main paper, which accurately models the experimental TPD traces. All three models yield TPD traces with a pronounced maximum at intermediate coverages and thus resemble the experimental data more strongly than all of the above discussed models with different prefactors. This shows that it is the prefactor that determines the shape of the TPD traces, as we obtain spectra that qualitatively resemble the shape of the experimental TPD traces very well even with an almost constant desorption energy (cf. Fig. S6 (g)).

In summary, Fig. S6 shows that our experimental TPD traces can only be modeled accurately with a kink in the coverage dependence of the prefactor. Its kink is the parameter that determines the shape of the TPD traces, whereas the desorption energy only leads to an additional broadening of the TPD traces and a change of the absolute desorption temperatures.

8. Scanning tunneling microscopy data of monolayers of PEN/Au(111) and PFP/Au(111)
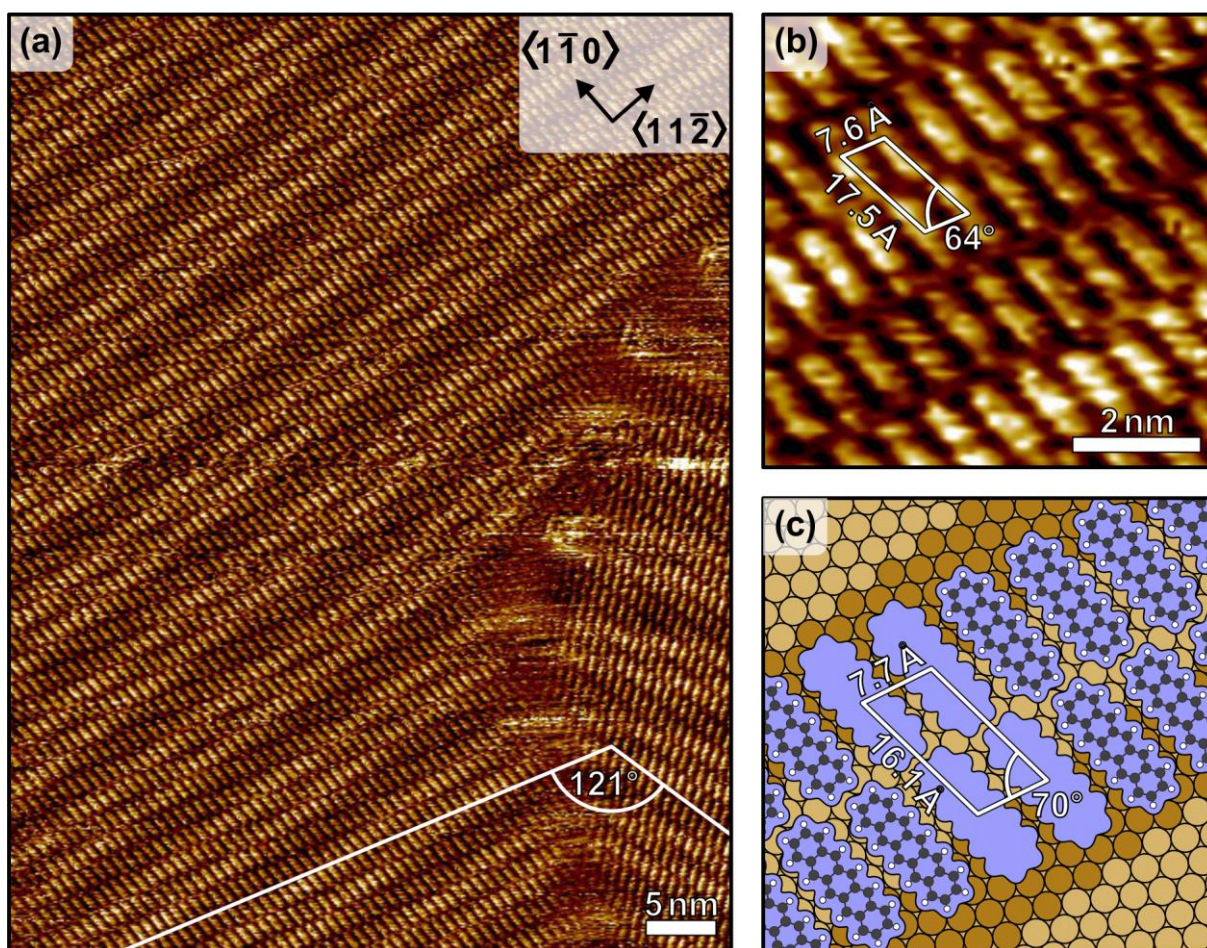

Fig. S7: (a) STM micrograph (0.98 V, 20 pA, 110 K) of a monolayer of PEN/Au(111) that was prepared by controlled annealing of a multilayer film (nominal thickness 7 nm, 420 K for 5 min). (b) Magnification of the micrograph with the unit cell highlighted. (c) Illustration of the $\begin{pmatrix} 6 & -1 \\ -2 & 3 \end{pmatrix}$ superstructure.

Figs. S7 and S8 show large-scale STM micrographs of monolayers of PEN/Au(111) and PFP/Au(111), respectively, together with magnifications that show the unit cell of the molecular monolayers and structural models based on the STM data and recently published LEED data on such films.[S22] Both molecular monolayers shown here were created by controlled annealing of molecular multilayers with a nominal thickness of 7 nm (420 K for 5 min).

Both micrographs show large areas of single crystalline domains, as well as a domain boundary between two rotational domains. The angle of approximately 60° / 120° between these rotational domains can be attributed to the threefold symmetry of the Au(111) substrate. In both micrographs, we observe the characteristic Au(111) surface reconstruction through the molecular adlayer, which allows to identify the substrate azimuths.
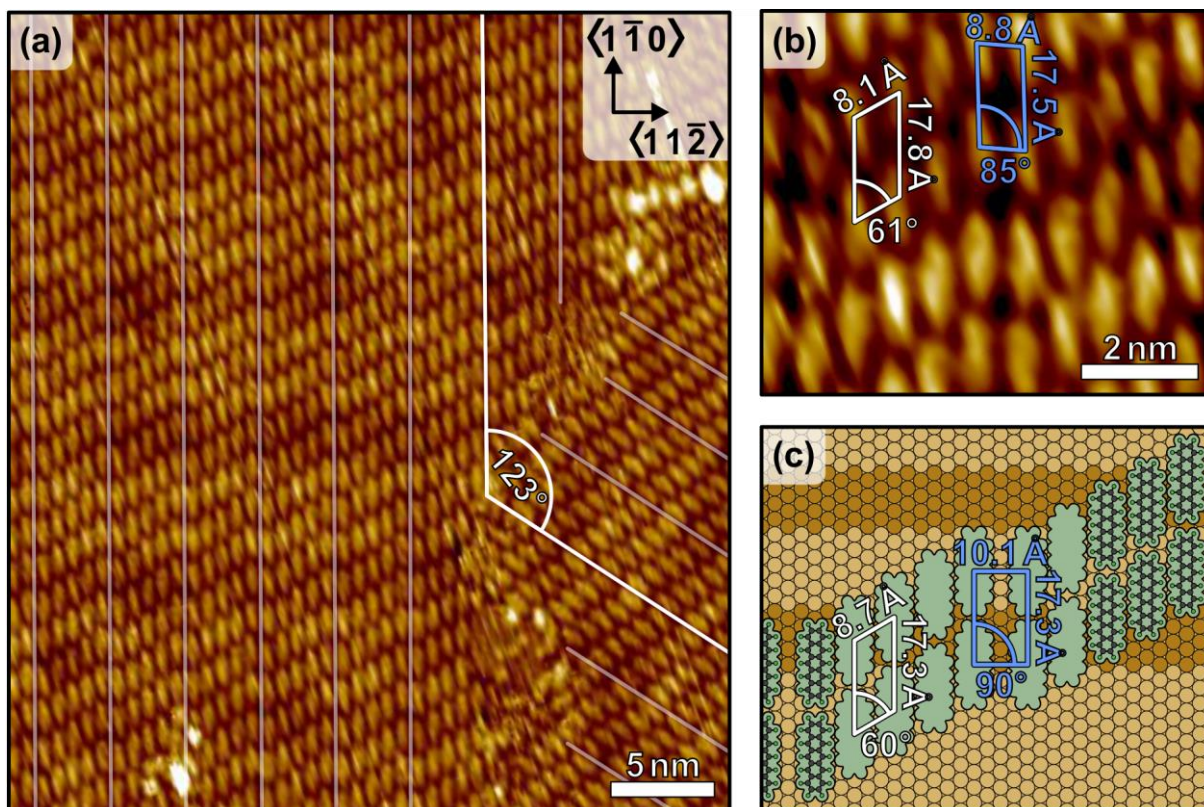
Fig. S8: (a) STM micrograph (1.85 V, 20 pA, 110 K) of a monolayer of PFP/Au(111) that was prepared by controlled annealing of a multilayer film (nominal thickness 7 nm, 420 K for 5 min). (b) Magnification of the micrograph with the unit cell highlighted. (c) Illustration of the $\begin{pmatrix} 6 & 0 \\ 0 & 3 \end{pmatrix}$ superstructure with periodic dislocation lines.

For PEN/Au(111), we observe an oblique unit cell with a = 17.5±2 Å, b = 7.6±1 Å and γ = 64±10°. The angle between a and the $\langle 11\bar{2} \rangle_{\mathrm{Au}}$ azimuth is 78±10°. We find a small angle of 3±10° between the long molecular axis and the $\langle 1\bar{1}0 \rangle_{\mathrm{Au}}$ azimuth that could, considering the uncertainty of this value, be considered zero. This structure is in good agreement with the recently reported $\begin{pmatrix} 6 & -1 \\ -2 & 3 \end{pmatrix}$ superstructure with unit cell parameters of a = 16.1 Å, b = 7.7 Å and γ = 70° that is shown in the structural model in Fig. S7 (c).[S22] The blue outlines of the molecules in this illustration show the van der Waals (vdW) boxes of the molecules. We find that, in order to avoid overlap of neighboring vdW boxes, molecules have to be rotated by approximately 5° between their long axis and the $\langle 1\bar{1}0 \rangle_{\mathrm{Au}}$, in line with the small measured angle.

For PFP/Au(111), we observe highly periodic dislocation lines that are highlighted by transparent white lines in Fig. S8 (a). Like the long molecular axes, these lines are oriented along the $\langle 1\bar{1}0 \rangle_{\mathrm{Au}}$ azimuth. The dislocation lines occur with a periodicity of five unit cells along the short unit vector. For the regular unit cell, we find a = 17.8±2 Å, b = 8.1±1 Å and γ = 61±10° with an angle of 93±10° between a and the $\langle 11\bar{2} \rangle_{\mathrm{Au}}$ azimuth. This oblique unit cell is in perfect agreement with the recently reported $\begin{pmatrix} 6 & 0 \\ 0 & 3 \end{pmatrix}$ superstructure with unit cell parameters of a = 17.3 Å, b = 8.7 Å and γ = 60°.[S22] At the dislocation lines, we find a rectangular quasi unit cell with a_{dis} = 17.5±2 Å, b_{dis} = 8.8±1 Å and γ_{dis} = 85±10°. We have included these dislocation lines

in our structure model (cf. Fig. S8 (c)) by shifting every sixth unit cell (along the short unit vector) to the next equivalent adsorption site along the $\langle 11\bar{2}\rangle_{\mathrm{Au}}$ azimuth. This yields a rectangular quasi unit cell with a_{dis} = 17.3 Å, b_{dis} = 10.1 Å and γ_{dis} = 90°, in good agreement with the measured parameters. Note that such periodic dislocation lines are also reported for the structurally very similar system of PFP/Ag(111), where they are attributed to lateral strain caused by a reduction of the preferred intermolecular distance in favor of the formation of a commensurate superstructure.[S23] This can also be seen in the structure model in Fig. S8 (c) where distances between neighboring vdW boxes are relatively small.

9. Influence of the molecular moments of inertia on the entropic stabilization

The comparison of the desorption kinetics of PEN and PFP provides an interesting opportunity to investigate experimentally on the influence of the molecular mass, or moment of inertia, on the partition functions for molecular rotation and thus the entropic stabilization. The rotational partition function can be calculated according to eqn S18:[S24,S25]

$$z_{\text{rot}}^{\text{ads}} = \frac{1}{\sigma} \left(\frac{8\pi k_B T}{h^2} \right)^{1/2} (I_z)^{1/2} . \qquad (S18)$$

Here, σ is a symmetry factor (σ = 2 for PEN and PFP), k_B is Boltzmann's constant, T is the temperature, h is Planck's constant and I_z is the molecule's moment of inertia for rotation around an axis perpendicular to the surface through its centre of mass.

From the rotational partition function, we can calculate the energetic stabilization of the system gained by rotational entropy according to eqn S19:[S25]

$$T \cdot \bar{S}_{\text{rot}}^{\text{ads}} = k_B T \left[\frac{1}{2} + \ln\left(z_{\text{rot}}^{\text{ads}} \right) \right]. \qquad (S19)$$

I_z can be calculated from the atomic coordinates within the molecule and the respective atomic masses. The atomic coordinates of PEN and PFP were calculated by means of density functional theory using an aug-cc-pVTZ basis set with the B3LYP functional as implemented in the US GAMESS-code.[S19,S20] The atomic coordinates are given in Tab. S4 for PEN and in Tab. S5 for PFP. With these values, we find I_z^{PEN} = 7.77·10⁻⁴⁴ kg m² and I_z^{PFP} = 2.05·10⁻⁴³ kg m². Thus, we find that, due to the higher mass of fluorine compared to hydrogen, the moment of inertia for in-plane rotation of PFP is 2.63 times larger than that of PEN.

Atom Nr.	Element	Coordinates x [Å]	y [Å]
1	C	0.000	1.395
2	C	1.233	0.727
3	C	2.481	1.394
4	C	3.699	0.728
5	C	4.962	1.407
6	C	6.131	0.712
7	F	0.000	2.731
8	F	2.485	2.731
9	F	5.016	2.742
10	F	7.307	1.339

Tab. S5: Atomic coordinates for a PFP molecule. Atomic labels correspond to Fig. S5.

Plugging these moments of inertia into eqn S18, we obtain rotational partition functions of 78.4 and 127.3 for PEN and PFP, respectively, at a temperature of T = 400 K, i.e., at the onset of monolayer desorption. Plugged into eqn S19, these values yield entropic stabilizations due to rotation of 0.168 eV = 16.2 kJ/mol and 0.184 eV = 17.8 kJ/mol for PEN and PFP, respectively,

again assuming a temperature of 400 K. Thus, even though its mass is almost twice as high as that of PEN and its moment of inertia is larger by a factor of 2.6, the entropic stabilization of PFP is only 9.5% larger than that of PEN.

Unfortunately, due to the partial decomposition of PFP during desorption from the Au(111) surface, we cannot compare the entropic stabilization gained from in-plane rotation of the two molecules from the data presented in this work. However, in a previous study on the desorption kinetics of PEN/MoS$_2$(0001) and PFP/MoS$_2$(0001),[S26] no molecular decomposition occurred and we were able to determine the entropic stabilization of both molecules with respect to the immobile multilayer phases *via* the standard Gibbs free energies of the respective phases. We found entropic stabilizations of 19±5 kJ/mol = 0.20±0.05 eV and 26±5 kJ/mol = 0.27±0.05 eV for PEN and PFP, respectively, at a temperature of 400 K. The experimentally determined entropic stabilization is therefore 37±45 % larger for PFP than for PEN, in line with the above discussed theoretical expectation based on the molecular moments of inertia.

10. <u>References</u>

S1. S. Müllegger and A. Winkler, *Surf. Sci.*, 2006, **600**(6), 1290.

S2. P. Frank, N. Koch, M. Koini, R. Rieger, K. Müllen, R. Resel and A. Winkler, *Chem. Phys. Lett.*, 2009, **473**(4-6), 321.

S3. D. Käfer, L. Ruppel and G. Witte, *Phys. Rev. B*, 2007, **75**(8), 3.

S4. S. Duhm, S. Hosoumi, I. Salzmann, A. Gerlach, M. Oehzelt, B. Wedl, T.-L. Lee, F. Schreiber, N. Koch, N. Ueno and S. Kera, *Phys. Rev. B*, 2010, **81**(4).

S5. E. V. Kornelsen, *Can. J. Phys.*, 1964, **42**(2), 364.

S6. J. Yang, W. Cui, Y. Li, G. Xie, N. Zhang, R. Wang, T. Hu and H. Zhang, *Appl. Surf. Sci.*, 2016, **382**, 88.

S7. D. Edwards, *J. Appl. Phys.*, 1975, **46**(4), 1437.

S8. J. B. Miller, H. R. Siddiqui, S. M. Gates, J. N. Russell, J. T. Yates, J. C. Tully and M. J. Cardillo, *J. Chem. Phys.*, 1987, **87**(11), 6725.

S9. D. L. S. Nieskens, A. P. van Bavel and J. W. Niemantsverdriet, *Surf. Sci.*, 2003, **546**(2-3), 159.

S10. C. Schmidt, T. Breuer, S. Wippermann, W. G. Schmidt and G. Witte, *J. Phys. Chem. C*, 2012, **116**(45), 24098.

S11. Note that, while the first layer of PEN/Au(111) adsorbs coplanar on the Au(111) surface, subsequent layers adopt a herringbone packing motif that has a different packing density. Therefore, our coverage-normalization is only accurate for the first monolayer.

S12. F. Widdascheck, A. A. Hauke and G. Witte, *Adv. Funct. Mater.*, 2019, **29**(17), 1808385.

S13. N. Koch, A. Vollmer, S. Duhm, Y. Sakamoto and T. Suzuki, *Adv. Mater.*, 2007, **19**(1), 112.

S14. P. G. Schroeder, C. B. France, J. B. Park and B. A. Parkinson, *J. Appl. Phys.*, 2002, **91**(5), 3010.

S15. J. R. Macdonald and C. A. Barlow, *J. Chem. Phys.*, 1963, **39**(2), 412.

S16. W. Kohn and K.-H. Lau, *Solid State Commun.*, 1976, **18**(5), 553.

S17. I. Kröger, B. Stadtmüller, C. Wagner, C. Weiss, R. Temirov, F. S. Tautz and C. Kumpf, *J. Chem. Phys.*, 2011, **135**(23), 234703.

S18. R. S. Mulliken, *J. Chem. Phys.*, 1955, **23**(10), 1833.

S19. M. W. Schmidt, K. K. Baldridge, J. A. Boatz, S. T. Elbert, M. S. Gordon, J. H. Jensen, S. Koseki, N. Matsunaga, K. A. Nguyen, S. Su, T. L. Windus, M. Dupuis and J. A. Montgomery, *J. Comput. Chem.*, 1993, **14**(11), 1347.

S20. M. S. Gordon and M. W. Schmidt in *Theory and applications of computational chemistry: The first forty years*, ed. C. E. Dykstra, Elsevier, Boston, Mass., 2005, p 1167.

S21. P. A. Redhead, *Vacuum*, 1962, **12**(4), 203.

S22. Q. Wang, J. Yang, A. Franco-Cañellas, C. Bürker, J. Niederhausen, P.-M. Dombrowski, F. Widdascheck, T. Breuer, G. Witte, A. Gerlach, S. Duhm and F. Schreiber, *Nanoscale Adv.*, 2021, **3**, 2598.

S23. J. Götzen, C. H. Schwalb, C. Schmidt, G. Mette, M. Marks, U. Höfer and G. Witte, *Langmuir*, 2011, **27**(3), 993.

S24. M. Roos, A. Breitruck, H. E. Hoster and R. J. Behm, *Physical chemistry chemical physics PCCP*, 2010, **12**(4), 818.

S25. T. Waldmann, J. Klein, H. E. Hoster and R. J. Behm, *ChemPhysChem*, 2013, **14**(1), 162.

S26. S. R. Kachel, P.-M. Dombrowski, T. Breuer, J. M. Gottfried and G. Witte, *Chem. Sci.*, 2021, **12**, 2575.